The Astrophysical Journal, 810:45 (13pp), 2015 September 1 doi:10.1088/0004-637X/810/1/45

QUASI-PERIODIC FLUCTUATIONS AND CHROMOSPHERIC EVAPORATION IN A SOLAR FLARE RIBBON OBSERVED BY *IRIS*

Jeffrey W. Brosius[1] and Adrian N. Daw[2]
[1] Catholic University of America at NASA Goddard Space Flight Center, Solar Physics Laboratory, Code 671, Greenbelt, MD 20771, USA; Jeffrey.W.Brosius@nasa.gov
[2] NASA Goddard Space Flight Center, Solar Physics Laboratory, Code 671, Greenbelt, MD 20771, USA
Received 2015 April 24; accepted 2015 July 23; published 2015 August 27

ABSTRACT

The Interface Region Imaging Spectrograph (*IRIS*) satellite obtained rapid cadence (9.4 s) stare spectra of an M7 flare ribbon in AR 12036 on 2014 April 18. Chromospheric and transition region line emission exhibited quasi-periodic intensity and velocity fluctuations in the ribbon prior to the appearance of Fe XXI emission. Seven intensity peaks were observed in light curves from small ($0\farcs333 \times 0\farcs333$) tracked spatial locations in the ribbon, the first four of which show variable time separations around 3 minutes, and the last four of which show variable time separations about half that value, i.e., the frequency appears to have doubled. The Fe XXI intensity increased rapidly and impulsively after the quasi-periodic fluctuations in chromospheric and transition region lines. The entire Fe XXI line profile was blueshifted when the line first appeared, corresponding to an upward velocity around -100 km s^{-1}. This upward velocity increased to a maximum of about -150 km s^{-1} before diminishing to zero around the time of maximum intensity. Simultaneous, cospatial velocities observed with Si IV line emission were directed downward, consistent with explosive chromospheric evaporation. During this flare the Fe XXI line's profile is well fit with only one Gaussian component that is either wholly blueshifted or wholly at rest; no significant secondary blueshifted or redshifted components are observed. This suggests that *IRIS* may have sufficient spatial resolution to resolve loop strands in these flare observations. Under the assumption that the Fe XXI line is at rest when its width is thermal, we derive a rest wavelength of 1354.0714 $\pm$ 0.0108 Å for this forbidden line.

Key words: Sun: activity – Sun: chromosphere – Sun: flares – Sun: UV radiation

1. INTRODUCTION

In the standard model of solar flares (Carmichael 1964; Sturrock 1968; Hirayama 1974; Kopp & Pneuman 1976), energy stored in twisted and stressed coronal magnetic fields is released by reconnection. This energy heats the plasma near the reconnection site to temperatures $T \gtrsim 10$ MK (i.e., "flare" temperatures) and/or accelerates nonthermal particles, and is subsequently transported by thermal conduction and/or particle beams through the relatively tenuous corona to the chromosphere, where it is stopped in the cooler, denser plasma. Alfvén waves have also been proposed to transport energy to the chromosphere (Fletcher & Hudson 2008; Haerendel 2009). At present it is not known how the released magnetic energy is partitioned among heat, beams, and waves. The possibility that reconnection occurs in the chromosphere has also been presented (Fang et al. 2006; Brosius & Holman 2009; Brosius 2013b; Ni et al. 2015).

If the flare energy flux into the chromosphere exceeds what can be shed by radiative losses, the chromosphere will heat and expand. Heated chromospheric material expands upward into the (less dense) corona, ultimately filling loops that appear as hot, dense, thermal flare structures. This process, first described by Neupert (1968), has become known as "chromospheric evaporation" (see reviews by Bornmann 1999; Fletcher et al. 2011). Blueshifts $\gtrsim$100 km s^{-1} in emission lines formed at flare temperatures provide evidence for this phenomenon (Antonucci et al. 1982, 1999; Doschek 1983; Mariska et al. 1993; Brosius 2003, 2013a; Brosius & Phillips 2004; Teriaca et al. 2003, 2006; Doschek et al. 2013; Young et al. 2013; Tian et al. 2014). Evaporation proceeds "explosively" when emission lines formed at flare temperatures appear blueshifted while emission lines formed in the chromosphere and transition region appear redshifted ($\sim$20–40 km s^{-1}); evaporation proceeds "gently" when emission lines formed in the chromosphere and transition region (as well as hotter lines, if observed) all appear blueshifted $\sim$20–40 km s^{-1} (Fisher et al. 1985; Brosius & Phillips 2004; Allred et al. 2005; Milligan et al. 2006a, 2006b; Brosius 2009).

Quasi-periodic fluctuations are an intrinsic part of flares (Nakariakov & Melnikov 2009), and have been observed in the light curves of all electromagnetic bands associated with flare-generated emission (Inglis & Nakariakov 2009). A likely cause of quasi-periodic fluctuations is time variability in the charged-particle acceleration process, such as would be the case if magnetic reconnection proceeded quasi-periodically (Nakariakov et al. 2010). There are two possible explanations for this occurrence (Inglis & Nakariakov 2009; Nakariakov & Melnikov 2009; Nakariakov et al. 2010): (1) magnetic energy continuously builds up in the vicinity of the flare epicenter (perhaps due to photospheric motions twisting and stressing magnetic field lines that extend into the corona) until a certain critical level (dictated by plasma conditions in and near the reconnection site) is reached, at which time the energy is released in a burst, and the process repeats; (2) the release of magnetic energy is periodically triggered by an external resonator (perhaps due to modulations produced by MHD waves or oscillations) for which the periodicity is prescribed either by certain resonances or by dispersive narrowing of initially broad spectra. There are a vast variety of mechanisms, all of which yield similar observational manifestations, that can produce quasi-periodic fluctuations in flares. Identifying the specific mechanism responsible for any given observed quasi-periodic fluctuation event is a non-trivial task (Inglis & Nakariakov 2009; Nakariakov & Melnikov 2009).

Quasi-periodic intensity fluctuations have been observed in flare chromospheric emission with a number of ground-based instruments. Wang et al. (2000) used Hα–1.3 Å images of a C5.7 flare observed at a cadence of 0.033 s at Big Bear Solar Observatory (BBSO) to detect fluctuations on timescales of 0.3 to 0.7 s in one of the flare kernels during the impulsive phase. They associated these high-frequency fluctuations with electron acceleration and precipitation at the footpoint of a flare loop. McAteer et al. (2005) used Hα–0.3 Å images of a C9.6 flare observed at a cadence of 0.083 s at BBSO to find periods of 40–80 s in a flare ribbon during the impulsive phase. These were interpreted in terms of flare-induced acoustic waves along a series of overlying loops. Jackiewicz & Balasubramaniam (2013) used Hα line center images observed at a cadence of 1 minute at the USAF/NSO Improved Solar Observing Optical Network to detect filament oscillations activated by chromospheric oscillations in distant flares. Keys et al. (2011) used Hα (6562.8 Å) and Ca II K (3934.2 Å) imaging spectroscopy measurements of a C2.0 flare observed at the Swedish Solar Telescope on La Palma to detect flare bursts with a period around 60 s. Spectroscopic information enabled them to derive line-of-sight Hα Doppler velocities of the flare ribbon with an effective cadence of 63 s, which revealed both redshifted and blueshifted velocities up to 17 km s^{-1}.

Here we present UV stare spectra of a solar flare ribbon observed by the *Interface Region Imaging Spectrograph* (*IRIS*; De Pontieu et al. 2014) satellite. The observations feature quasi-periodic fluctuations in chromospheric and transition region line emission from the ribbon, followed by chromospheric evaporation. In Section 2 we describe the observations and our analysis of the spectra, in Section 3 we present our results regarding quasi-periodic fluctuations and chromospheric evaporation, in Section 4 we discuss implications of the results, and in Section 5 we summarize our conclusions.

2. OBSERVATIONS AND ANALYSIS

IRIS obtained stare spectra of AR 12036 (S20W34) from 12:33:38 until 17:18:01 UT during a *GOES* M7.3 flare that started at 12:31 and peaked at 13:03 UT on 2014 April 18. (The maximum in the *GOES* emission, which has no spatial resolution, was earlier than that seen in Fe XXI line emission at the location of the *IRIS* slit.) The duration of the 1818 *IRIS* Far-ultraviolet (FUV) stare exposures was 8 s, and the cadence of the observations was about 9.4 s. For this analysis we focus on the "O I 1356" and "Si IV 1403" FUV windows. The former covers wavelengths from 1352.3500 to 1356.6853 Å, and includes the forbidden line of Fe XXI at 1354.066 Å (formed at temperature $T \approx 11$ MK), C I 1354.288, O I 1355.5977, C I 1355.844 Å, and several additional very weak lines discussed below; the latter covers wavelengths from 1398.7300 to 1406.3366 Å, and includes the Si IV line at 1402.772 Å (formed at $T \approx 0.079$ MK; this line is the strongest by far in this FUV window), several O IV lines (formed at $T \approx 0.14$ MK, the strongest of which is at 1401.157 Å), and S I 1401.5136 Å. The wavelengths that we list here for atomic emission lines are adopted from Kelly (1987), while those for ions are adopted from CHIANTI version 7.1.3 (Dere et al. 1997; Landi et al. 2013).

The data are the standard *IRIS* Level 2 science products in data number (DN) units, that is, ready for scientific analyses (McIntosh et al. 2014). Level 2 data processing includes corrections for dark current, pedestal offset, and flat field, along with geometric and wavelength calibrations. In addition to the FUV stare spectra, we analyze slit-jaw images (SJI) at 1400 Å. The SJI were recorded with variable exposure times that ranged from 8.0 s at the start to a minimum of 0.37 s during the flare. Even with the reduced flare exposure times, the SJI saturated particularly in the ribbon during the flare. This is not a problem here because we focus primarily on spectral data analysis in this work. None of the spectra in the O I 1356 window saturated during the observing run, but a few of the spectra in the Si IV 1403 window did, as described below.

The center of the 0.″333-wide slit, and hence the center of the SJI, was pointed at (+550.″7, −230.0) at the start of the observing run, with solar feature tracking for the entire observing sequence. Wobble compensation leaves a possible residual 2-pixel effect (De Pontieu et al. 2014) over the course of a full orbit (97 m), insignificant over the time interval spanning all the observed fluctuations (∼20 m). Examples of SJI are displayed in Figure 1. The spatial dimensions of the images are 724 × 774 spatial pixels, or 120.″4 × 128.″8. Spectra were obtained from the 774 spatial pixels along the slit in the y-direction, each of which is 0.″166 tall. Because the nominal instrumental spatial resolution is 0.″333, we averaged the spectra over two spatial pixels. Most of our analysis is based on these re-binned spectra.

The first frame of Figure 1 shows the first of 606 SJI 1400 Å images, in which the flare is readily seen to be already in progress (*GOES* observed it to begin about 2.5 minutes before the start of the *IRIS* observing run). The next three frames show images at later times during the flare, when ribbons are bright and prominent. Here we focus on spectra obtained in and near the portion of the ribbon observed by the slit, indicated by the yellow horizontal tick marks perpendicular to the slit in each frame. Note that the slit segment delineated by the yellow tick marks appears to be unaffected by the flare at the start of the *IRIS* observing run even though the flare had already begun and is evident south and east of this segment in the first 1400 Å SJI. The small blue box between the yellow ticks indicates the location of the ribbon when it first appeared across the slit. The intersection of the ribbon with the *IRIS* slit moved southward, at a rate of about 12″ hr^{-1}, or 2.5 km s^{-1}.

In order to derive reference wavelengths against which to calculate relative Doppler velocities during the flare, we formed a series of 18 spatially and temporally averaged slit spectra, hereafter referred to as "spacetime-averaged spectra," for both the O I 1356 and Si IV 1403 spectral windows. Each spectrum in the series was derived by averaging over the 20.″1 segment of the slit (0.″166 spatial pixels 600–720, i.e., between the yellow tick marks in Figure 1) for successive sequences of 101 exposures (each about a 15.6 minute interval), covering almost the entire 1818-exposure run. This greatly reduces the noise relative to that in any individual spectrum, while retaining the ability to determine whether there may be systematic time-dependent effects that could affect our results. Reference wavelengths derived from these spectra are not necessarily the rest wavelengths of the lines, but rather the wavelengths measured by *IRIS* under quiescent solar conditions. Thus the velocities that we observe during the flare are not necessarily absolute, but are measured relative to these conditions.

2.1. The IRIS "O I 1356" Waveband

The spacetime-averaged spectra reveal that we observe 10 different lines in the O I 1356 waveband at least some of the

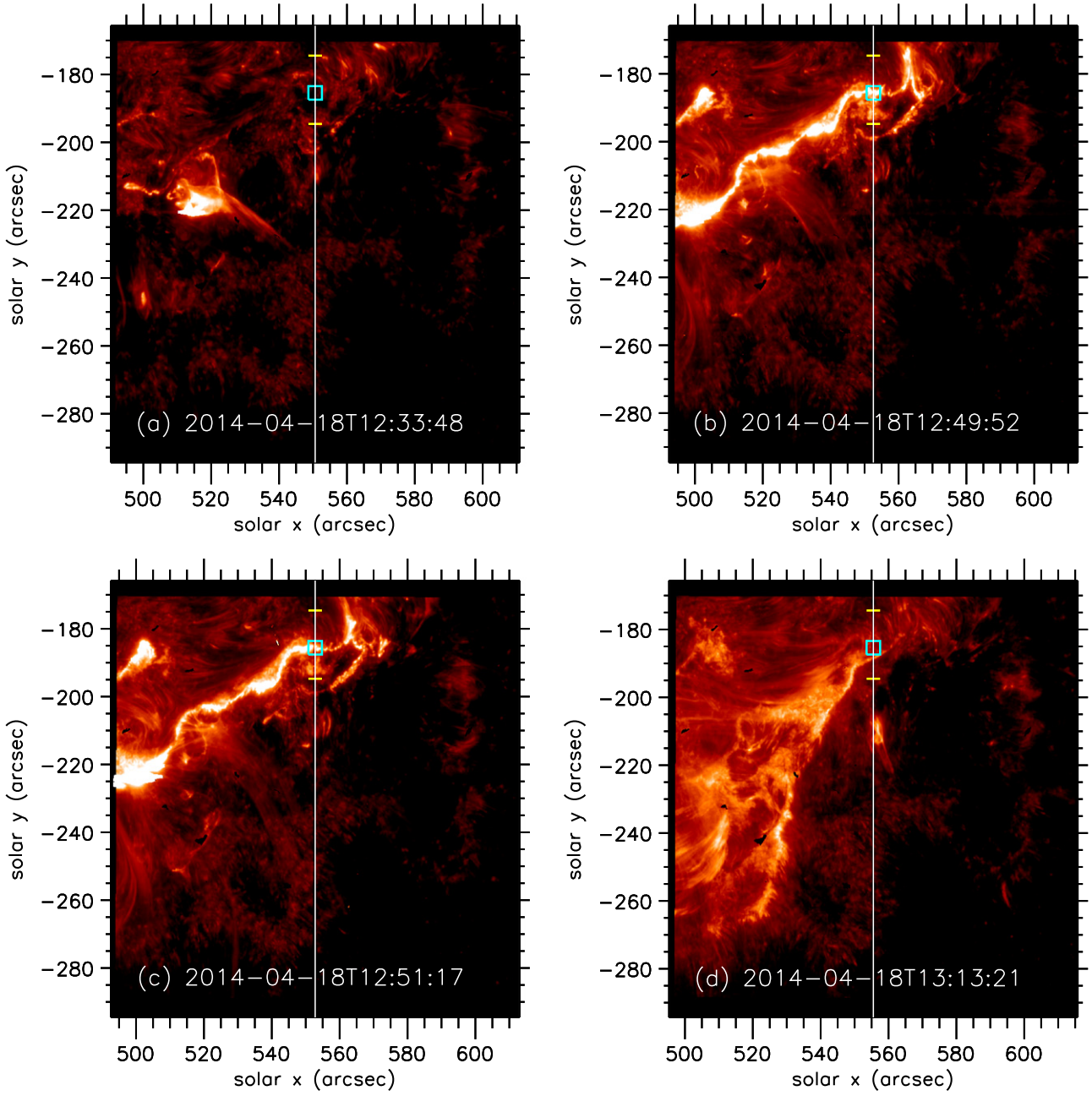

Figure 1. *IRIS* 1400 Å slit-jaw images obtained during the M7.3 flare of 2014 April 18. The (central) time at which each exposure was obtained is indicated in each frame. All images are displayed on the same intensity scale (DN s^{-1}). The images are centered around the pointing of the *IRIS* slit, which is overplotted as a white vertical line in each frame. The flare in AR 12036 started around 12:31 UT, and *IRIS* began staring at the region at 12:33:38 UT. The $4'' \times 4''$ blue box toward the top of each frame indicates the location of the flare ribbon when it first appeared at the location of the slit. Frame (a) shows the first *IRIS* slit-jaw image of the sequence, (b) shows the image at the first prominent intensity peak in slit spectra from the ribbon, (c) shows the image during the subsequent intensity trough, and (d) shows the image near the time of maximum Fe XXI emission observed within the box. Note that the flare ribbon intensity has diminished in (d), and that the ribbon has shifted southward. The yellow tick marks perpendicular to the slit indicate the segment (slit pixels 600 through 720) over which spectra were averaged to calculate reference wavelengths used to derive relative Doppler velocities.

time during the stare study (see also Young et al. 2015), with the two lines of C I and the one line of O I showing prominent redshifted components primarily while the ribbon is bright and active. Thus, the 13 components that we find in the series of spacetime-averaged spectra include Si II 1352.635 Å, Fe II 1353.023, Si II 1353.718, Fe II 1354.013, Fe XXI 1354.066, C I 1354.288 (which sometimes has a red component), Fe II 1354.747, Fe II 1354.87, O I 1355.5977 (which sometimes has a red component), and C I 1355.844 Å (which sometimes has a red component). All of the wavelengths listed here are again taken from Kelly (1987) and CHIANTI version 7.1.3. It is possible that the Si II and Fe II lines all have redshifted components sometime during the observing run, but they are too weak to reliably distinguish such emission from the single, main component.

Figure 2 shows sample spectra from the O I 1356 waveband at three different times during the observing run, including (a), (b) an average over the interval from 33 to 48 minutes after the flare's maximum observed by *GOES*, (c), (d) a time when chromospheric emission from the flare ribbon was particularly

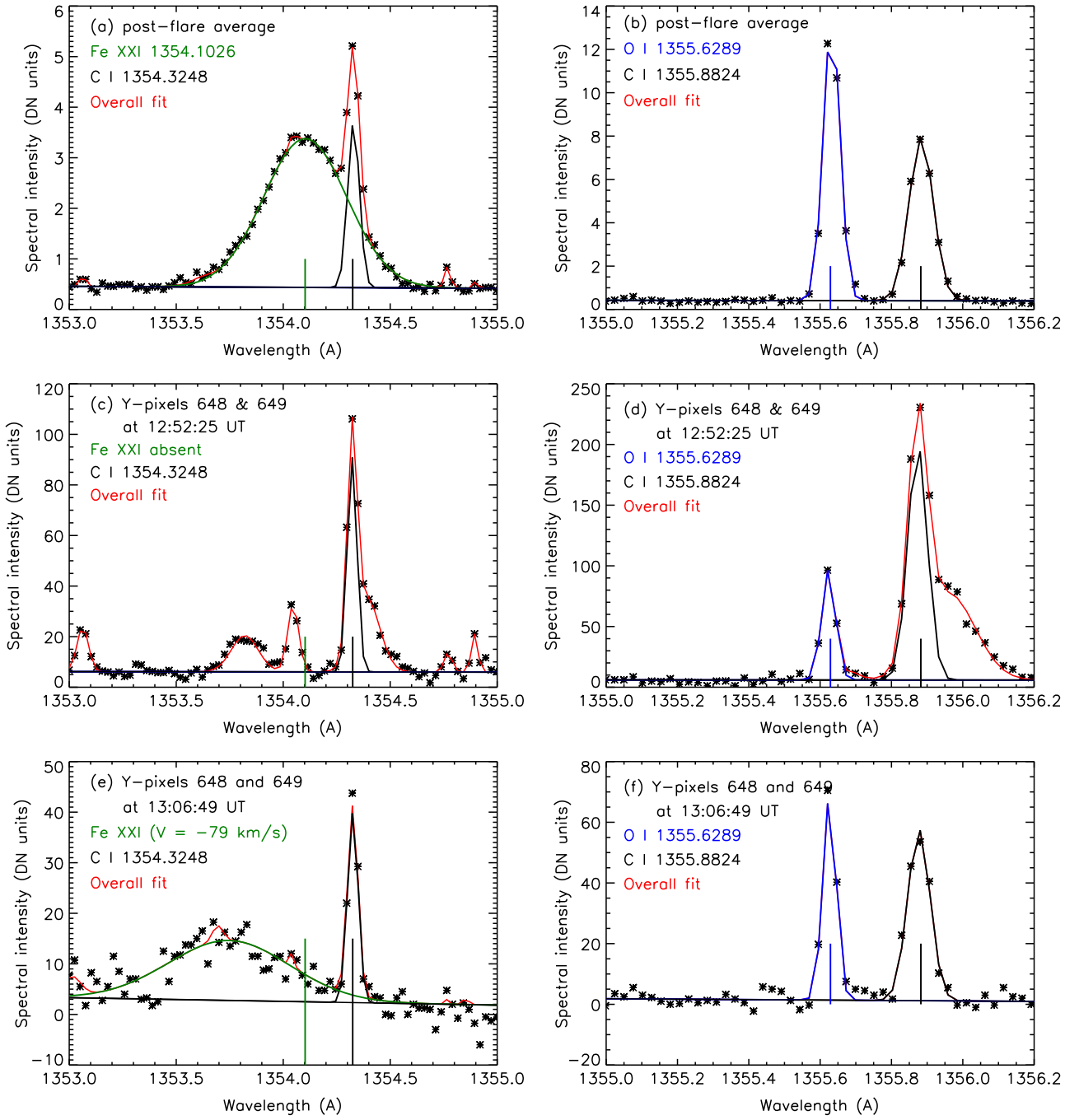

Figure 2. Sample spectra from the *IRIS* O I 1356 waveband. Frames (a) and (b) show the spectrum spatially averaged over the 20.″1 slit segment comprised of spatial pixels 600 through 720 during exposures 400 through 500 (13:36:15–13:51:54 UT, i.e., 33–48 minutes after the flare's maximum observed with *GOES*). Frames (c) and (d) show the spectrum from exposure 120 (12:52:25 UT) averaged over spatial pixels 648 and 649. Frames (e) and (f) show the spectrum from exposure 212 (13:06:49 UT) averaged over spatial pixels 648 and 649. Lines are color-coded as indicated in each frame, and their corresponding "reference" wavelengths, derived as described in the text, are overplotted and listed. In frames (a) and (b) the lines are at rest; in (c) and (d) Fe XXI emission is not observed, and the C I and O I lines each show a redshifted component (note the humps in the overall fit on the redward side of each line); in (e) the Fe XXI line is blueshifted.

bright, and (e, f) a time when the Fe XXI emission was increasing and the line's wavelength was blueshifted. The left column of Figure 2, frames (a), (c), and (e), show the wavelength range 1353.0–1355.0 Å, while the right column of Figure 2, frames (b), (d), and (f), show 1355.0–1356.2 Å. Note the different intensity scales in the two columns. Frames (a) and (b) show the spacetime-averaged spectrum from exposures 400 through 500, obtained between 13:36:15 and 13:51:54 UT, during which time the Fe XXI emitting source was at rest; frames (c) and (d) show the spectrum from exposure 120 (12:52:25 UT) averaged over spatial pixels 648 and 649; frames (e) and (f) show the spectrum from exposure 212 (13:06:49 UT) averaged over the same two pixels. Gaussian profile fits to selected emission lines are color-coded as indicated, and their corresponding "reference" wavelengths (described below) are marked. The sum of Gaussian profile fits to all spectral lines in the waveband (plus a linear background) is overplotted in red as the "overall fit;" this fit is evident only

where it differs from the color-coded fits to the individual lines listed and plotted in each frame. In other words, patches of red in each frame indicate the Fe II and Si II lines whose profile fits we do not specifically overplot with unique colors in the figure, as well as the redshifted components of the C I and O I lines, when they are significant. The Fe XXI, C I, and O I lines are at rest in frames (a) and (b). In frames (c) and (d) Fe XXI emission is not observed, and the C I and O I lines each show a redshifted component. In frame (e) the Fe XXI line is blueshifted. Note that the line of Si II at 1352.635 Å is outside the displayed range in Figure 2.

We fit each emission line (and secondary component in the case of C I and O I) in the spacetime-averaged spectra with a Gaussian profile using procedures developed by Haughan (1997). Uncertainties on spectral data points were obtained using the procedure described by Young et al. (2015), calculated as the quadrature sum of photon noise, read noise, and dark noise as described in De Pontieu et al. (2014). The resulting distribution of reduced chi squared values is consistent with that expected for Gaussian statistics: with typically 100 degrees of freedom per fit, 90% of reduced chi squared values fall between 0.7 and 1.3. Anomalously high values (>2) were the result of energetic particle hits on the CCD, and such data were excluded from the data set when line profile parameters were compromised as a result. Because (1) the secondary redshifted components that are sometimes prominently observed near the main C I and O I components can be weak and difficult to separate from the main component, and (2) determination of the presence or absence of the secondary "red" components can be subjective, we derive wavelengths λ for the C I and O I lines in each spectrum as intensity-weighted averages of the two components. This avoids any systematic effects that may be introduced by fitting the secondary components only some of the time, while not knowing exactly when or where such components need to be included.

Using this approach for the two C I lines and the one O I line, we derive reference wavelengths $\lambda_{\rm ref}$ of $\lambda_{\rm ref}$(C I) = 1354.3248 ± 0.0098 Å, $\lambda_{\rm ref}$(O I) = 1355.6289 ± 0.0101 Å, and $\lambda_{\rm ref}$(C I) = 1355.8824 ± 0.0104 Å, where each wavelength and its associated uncertainty covers the entire spread of values derived for each line from the 18 spacetime-averaged spectra. (Contributions from the flare fluctuation spectra do not affect these wavelength measurements for the C I and O I lines.) We repeated the reference wavelength derivation *excluding* the redshifted components to the C I and O I lines (which are most significant during the flare's impulsive phase), and find that the resulting reference wavelengths do not differ significantly from those derived above.

The Fe XXI line is significant in only 7 of the 18 averaged spectra, and of those 7 its width is comparable to its thermal value of 434 mÅ in 3 cases. (If we include the instrumental width of 25.85 mÅ given by De Pontieu et al. 2014, the minimum expected line width is 435 mÅ.) Assuming that the line is at rest when its width indicates that turbulence is negligible, we derive a reference wavelength of $\lambda_{\rm ref}$(Fe XXI) = 1354.1026 ± 0.0038 from these three spectra. These are the wavelengths that we use to calculate relative Doppler velocities in the spatially and temporally resolved spectra. The wavelength uncertainties correspond to velocity uncertainties around 2.2 km s^{-1} for the C I and O I lines, and around 1 km s^{-1} for Fe XXI.

Taking the 1355.5977 Å rest wavelength of the O I line (Edlen 1963; Kelly 1987) as a reliable standard, we see that our reference wavelength is 0.0312 Å longer than the standard value. Applying a corrective shift of −0.0312 ± 0.0101 Å to the measured reference wavelengths of the C I and Fe XXI lines, we derive rest wavelengths $\lambda_{\rm rest}$ for both C I lines that are consistent with the values given in Kelly (1987), and a rest wavelength for Fe XXI of 1354.0714 ± 0.0108 Å. Our Fe XXI rest wavelength is consistent with the value of 1354.0665 Å in CHIANTI v.7.1.3 (Dere et al. 1997; Landi et al. 2013) and 1354.08 Å in the NIST Atomic Spectra Database (Shirai et al. 2000), as well as with that of 1354.064 ± 0.020 Å reported by Feldman et al. (2000; based on Solar Ultraviolet Measurements of Emitted Radiation (SUMER) flare spectra above the limb), 1354.08 ± 0.05 Å reported by Sandlin et al. (1977; based on *Skylab* flare spectra at and near the limb), and 1354.106 ± 0.023 Å reported by Young et al. (2015; based on *IRIS* flare raster spectra), within the combined uncertainties of the two measurements.

Using the same line profile fit structure with 13 components (including the red components to the C I and O I lines) that was used for the spacetime-averaged spectra, we fit line profiles in the 126 two-pixel-averaged spectra covering a 41.″9 segment of the slit (*Y*-pixels 500 through 751) for the first 501 exposures in the series. Figure 3 shows space versus time "images" of the integrated line intensities and relative Doppler velocities for Fe XXI and C I 1355.8. Positive velocities correspond to redshifted wavelengths (downward motion, lighter colors), while negative velocities correspond to blueshifted wavelengths (upward motion, darker colors). A visual inspection of the images reveals that the C I intensity and velocity show quasi-periodic fluctuations (in which the velocity image generally indicates redshifts during the intervals of increased brightness) that precede the appearance of Fe XXI emission, and that Fe XXI is blueshifted when it first appears. Velocities derived for areas in which the line intensities are low (and hence appear dark in frames (a) and (c)) are mostly noise.

2.2. The IRIS "Si IV 1403" Waveband

We focus on the Si IV line at 1402.772 Å and the O IV line at 1401.157 Å to investigate the evolution of transition region emission during the observing run. The Si IV line saturated in slit pixels that crossed the flare ribbon for a few of the exposures during which the ribbon became very bright, particularly in slit *Y*-pixels 639 through 646 each for one or more of exposures 104 through 107, and slit *Y*-pixels 648 through 656 each for one or more of exposures 117 through 123. The worst of the saturated Si IV 1402.772 Å profiles have about 20 saturated spectral pixels, but most of the saturated profiles have fewer than that.

Figure 4 shows sample spectra from the Si IV 1403 waveband at three different times during the observing run, including (a), (b) near the end of the observing run, (c), (d) times when chromospheric emission from the flare ribbon was particularly bright, and (e), (f) a time when the Fe XXI emission was increasing (and its wavelength blueshifted). The left column of Figure 4, frames (a), (c), and (e), show the wavelength range 1400.8–1401.8 Å, while the right column of Figure 4, frames (b), (d), and (f), show 1402.0–1404.0 Å. Note the different intensity scales in the two columns. Frames (a) and (b) show the spacetime-averaged spectrum from exposures 1700 through 1800, obtained between 16:59:43 and 17:15:22 UT, during

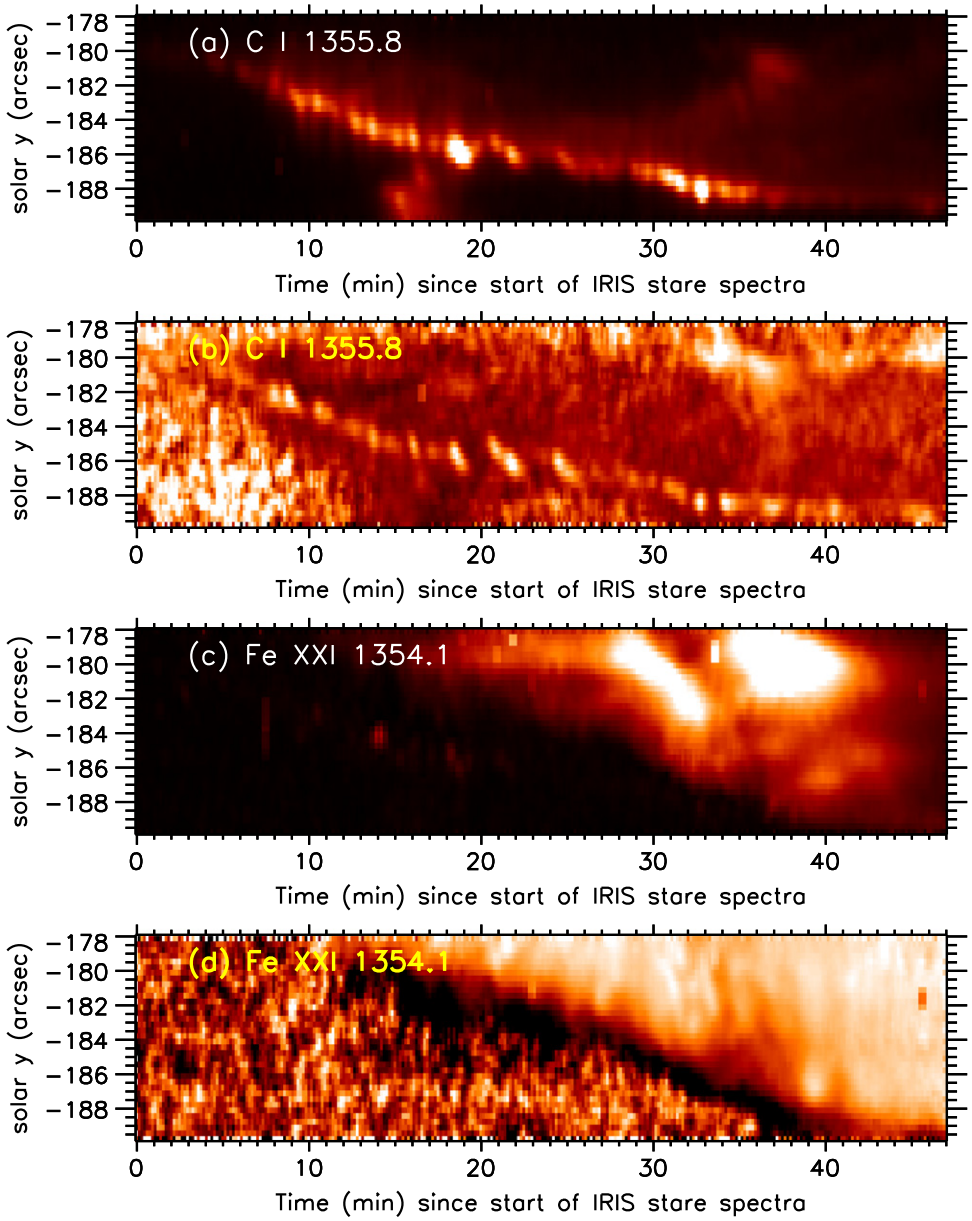

Figure 3. Space vs. time "image" arrays of intensity and relative Doppler velocity for the C I 1355.8 and Fe XXI 1354.1 Å emission lines observed by *IRIS*. The *x*-axis extends from 12:33:38 to 13:20:36 UT, and the *y*-axis covers a 12″ segment of the *IRIS* slit. Quasi-periodic fluctuations in the C I intensity and relative Doppler velocity are evident in frames (a) and (b); frames (c) and (d) show that Fe XXI is blueshifted (upward velocity is negative, and hence appears dark) when it first appears in the ribbon. Velocities in areas where the line intensities are low (and hence appear dark in frames (a) and (c)) are mostly noise.

which time the transition region appeared to be at rest; frame (c) shows the spectrum from exposure 120 (12:52:25 UT, the same as in Figure 2) averaged over spatial pixels 648 and 649, while frame (d) shows the spectrum from exposure 140 (12:55:33 UT, a time when the Si IV profile was not saturated) averaged over spatial pixels 648 and 649; frames (e) and (f) show the spectrum from exposure 212 (13:06:49 UT, the same as in Figure 2) averaged over spatial pixels 648 and 649.

In Figures 4(a), (c), (e), Gaussian profile fits to emission lines of O IV, S I, and an unidentified line between them are color-coded as indicated, and their corresponding reference wavelengths (described below) are marked. The sum of Gaussian profile fits to these and a couple of weak Fe II lines at wavelengths longward of the displayed range, plus a linear background, is overplotted in red as the "overall fit;" as with Figure 2 above, the red curve is evident where it differs from the color-coded fits to the individual lines listed and plotted in each frame. The O IV, S I, and unidentified lines are at rest in frame (a). The 18 spacetime-averaged spectra in this waveband show that the O IV wavelength fluctuates more than did the C I and O I wavelengths over the flare's long duration decline, possibly due to turbulence and flows in the transition region as flare-heated material cools and falls, but settles down near the end of the observing run: we use the last 3 spacetime-averaged spectra in the series to derive the O IV reference wavelength of 1401.1926 ± 0.0071 Å. (The wavelengths derived from the first 3 spacetime-averaged spectra in the series also all lie within this range.) For S I we get 1401.5364 ± 0.0060, and for the unidentified line we get

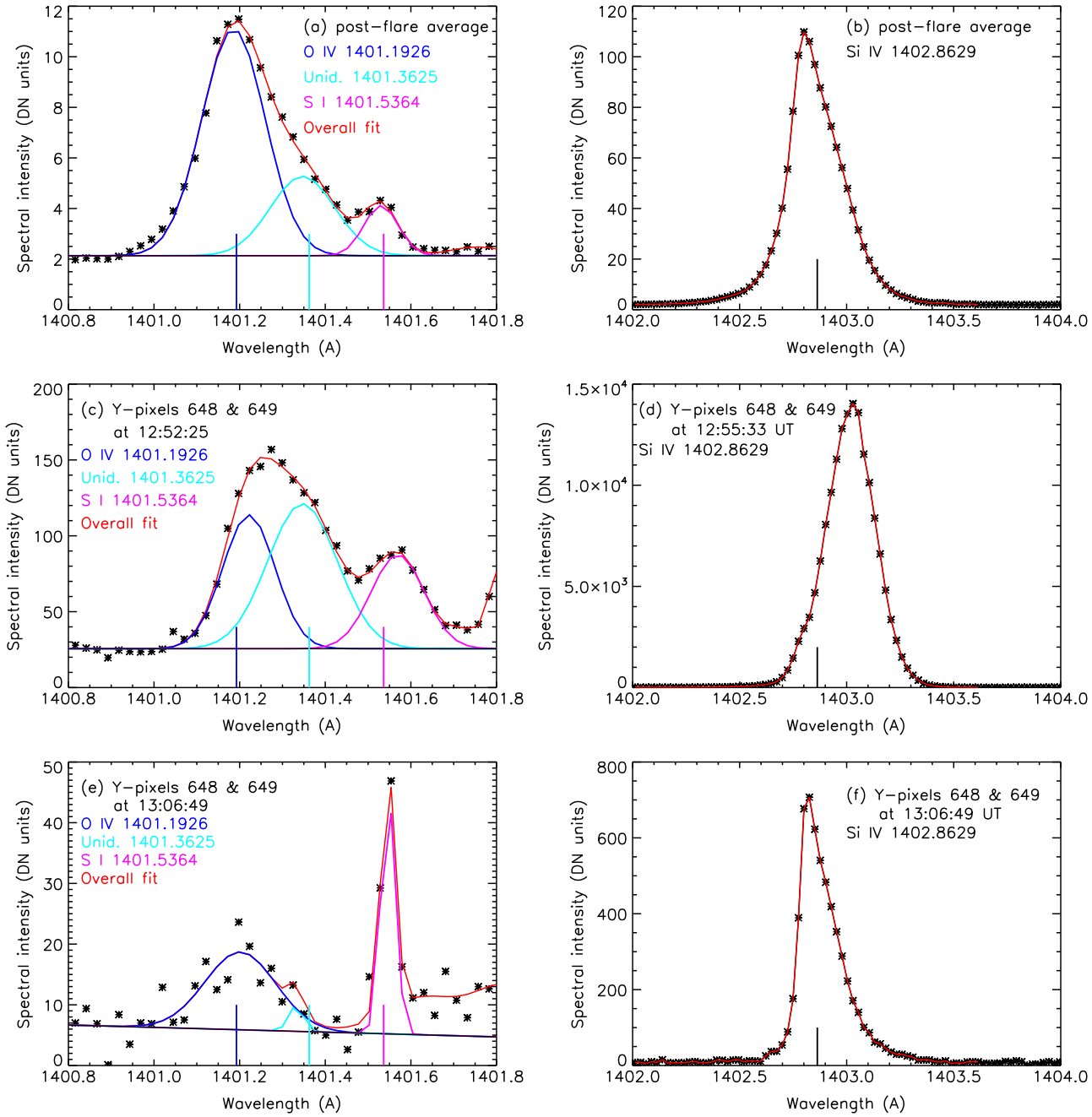

Figure 4. Sample spectra from the *IRIS* Si IV 1403 waveband. Frames (a) and (b) show the spectrum spatially averaged over the 20.″1 slit segment comprised of spatial pixels 600 through 720 during exposures 1700 through 1800 (16:59:43–17:15:22 UT, i.e., near the end of our observing run, by which time the transition region had become much less turbulent). Frame (c) shows the spectrum from exposure 120 (12:52:25 UT) while frame (d) shows that from 140 (12:55:33 UT), each averaged over spatial pixels 648 and 649. Frames (e) and (f) show the spectrum from exposure 212 (13:06:49 UT) averaged over spatial pixels 648 and 649. In frames (a), (c), and (e) the lines are color-coded as indicated, and their corresponding "reference" wavelengths are overplotted and listed. In frames (b), (d), and (f) the spectral range over which the Si IV line's integrated intensity and centroid wavelength were obtained is overplotted in red. The line's "reference" wavelength is overplotted.

1401.3625 ± 0.0154. Our initial suspicion that the unidentified line might be attributed to Fe II is ruled unlikely because of the relatively large difference between its wavelength and that of the nearest known Fe II line (1401.229 Å; Kelly 1987; Nave & Johansson 2013). The close proximity of the O IV, unidentified, and S I lines compromises their wavelength measurements particularly in the (noisier) spatially and temporally resolved spectra.

An examination of the Si IV 1402.772 Å emission line in the spacetime-averaged spectra as well as in the spatially and temporally resolved spectra reveals that the profile assumes comparatively complex shapes even during the long duration of the flare's decline. The profile typically does not conform to a simple Gaussian, possibly because of turbulence, barely-resolved upward and/or downward flows, or opacity effects. (The Fe XXI, C I, and O I lines in the O I 1356 waveband do not exhibit this behavior, which suggests that the transition region is more affected than the chromosphere by the long slow decline of the flare.) Because the Si IV profile is not readily fit with one or two Gaussian components, we adopt a different

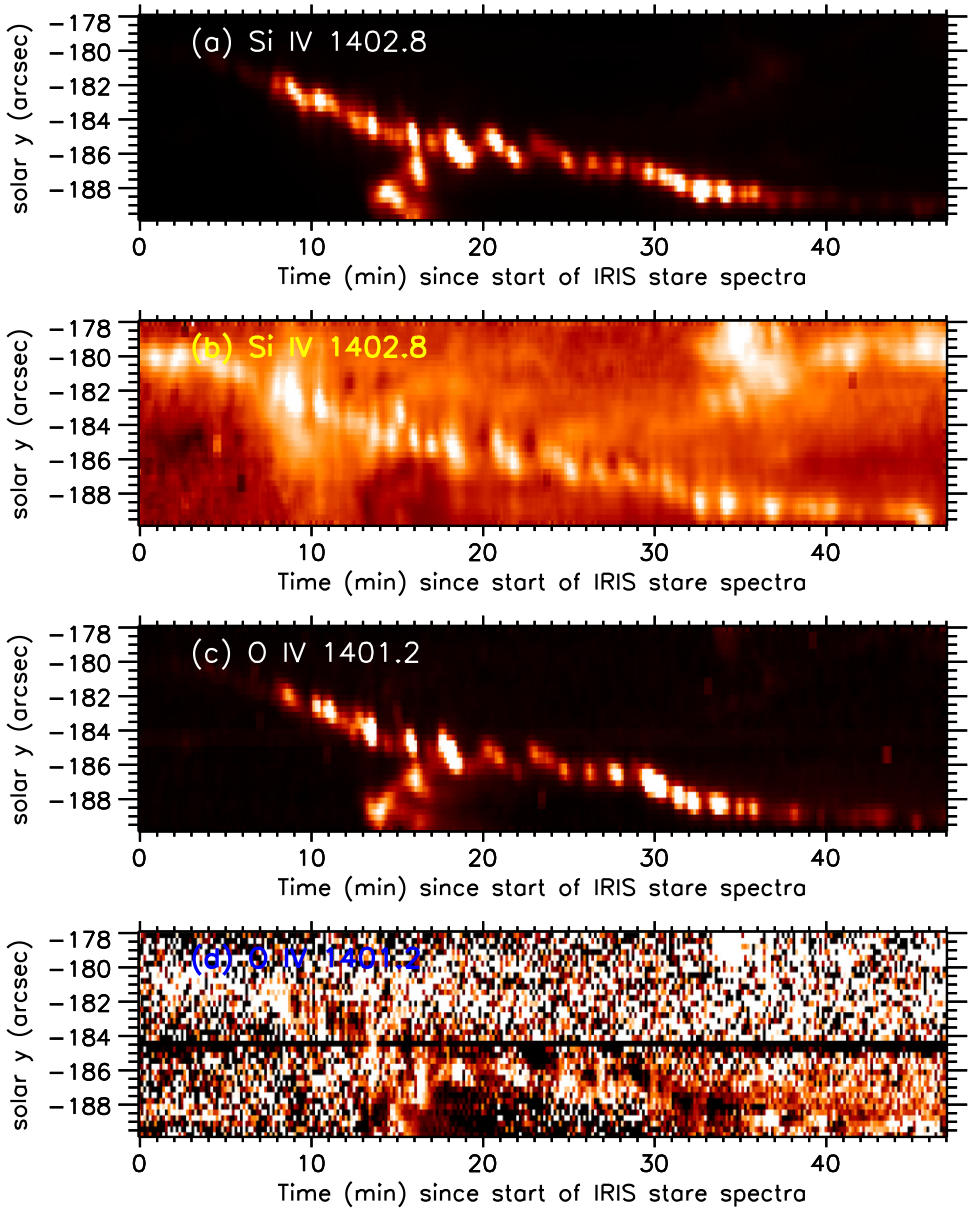

Figure 5. Space vs. time "image" arrays of intensity and relative Doppler velocity for the Si IV 1402.8 and O IV 1401.2 Å emission lines observed by *IRIS*. The *x*-axis extends from 12:33:38 to 13:20:36 UT, and the *y*-axis covers a 12″ segment of the *IRIS* slit. Quasi-periodic fluctuations in the Si IV intensity and relative Doppler velocity are evident in frames (a) and (b); they are also evident in the O IV intensity in frame (c), but difficult to see in the O IV velocity in frame (d). Velocities in areas where the line intensities are low (and hence appear dark) are mostly noise.

approach to measure its intensity and centroid wavelength during the flare. We sum the spectral intensity values in spectral pixel numbers 129–192 (1402.0118–1403.6145 Å, displayed in red in frames (b), (d), and (e)) surrounding the line's nominal rest wavelength to get the total (integrated) intensity. Similarly, we derive the intensity-weighted wavelength (the profile's centroid) by summing the products of the wavelength and corresponding spectral intensity values for the same spectral pixels over which the intensity was summed, and dividing this total by the summed intensity. Using the last 13 of the 18 spacetime-averaged spectra (13:51:54–17:15:22 UT), we derive a reference wavelength of 1402.8629 ± 0.0328 Å for Si IV. The long black vertical line in Figures 4(b), (d), (f) indicates the reference wavelength, compared to which it can be seen that the line is redshifted in frames (d) and (f).

We applied the above summation procedure to the re-binned spectra to obtain the space versus time arrays of Si IV 1402.8 Å intensity and relative Doppler velocity. These are displayed in Figures 5(a), (b), in which it can be seen that both quantities show quasi-periodic fluctuations. As with C I, the velocity image indicates redshifts during the intervals of increased brightness. Frames (c) and (d) show intensity and velocity "images" for O IV, for which the intensity shows quasi-periodic fluctuations but the velocity image shows a lot of scatter owing to the weakness of the line in the spatially and temporally resolved spectra, as well as to the nearby blends. Overall, Figures 3 and 5 (and the light curves displayed below) indicate that the chromosphere and the transition region are both involved in the flare *before* Fe XXI emission is observed from the ribbon at this location along the slit.

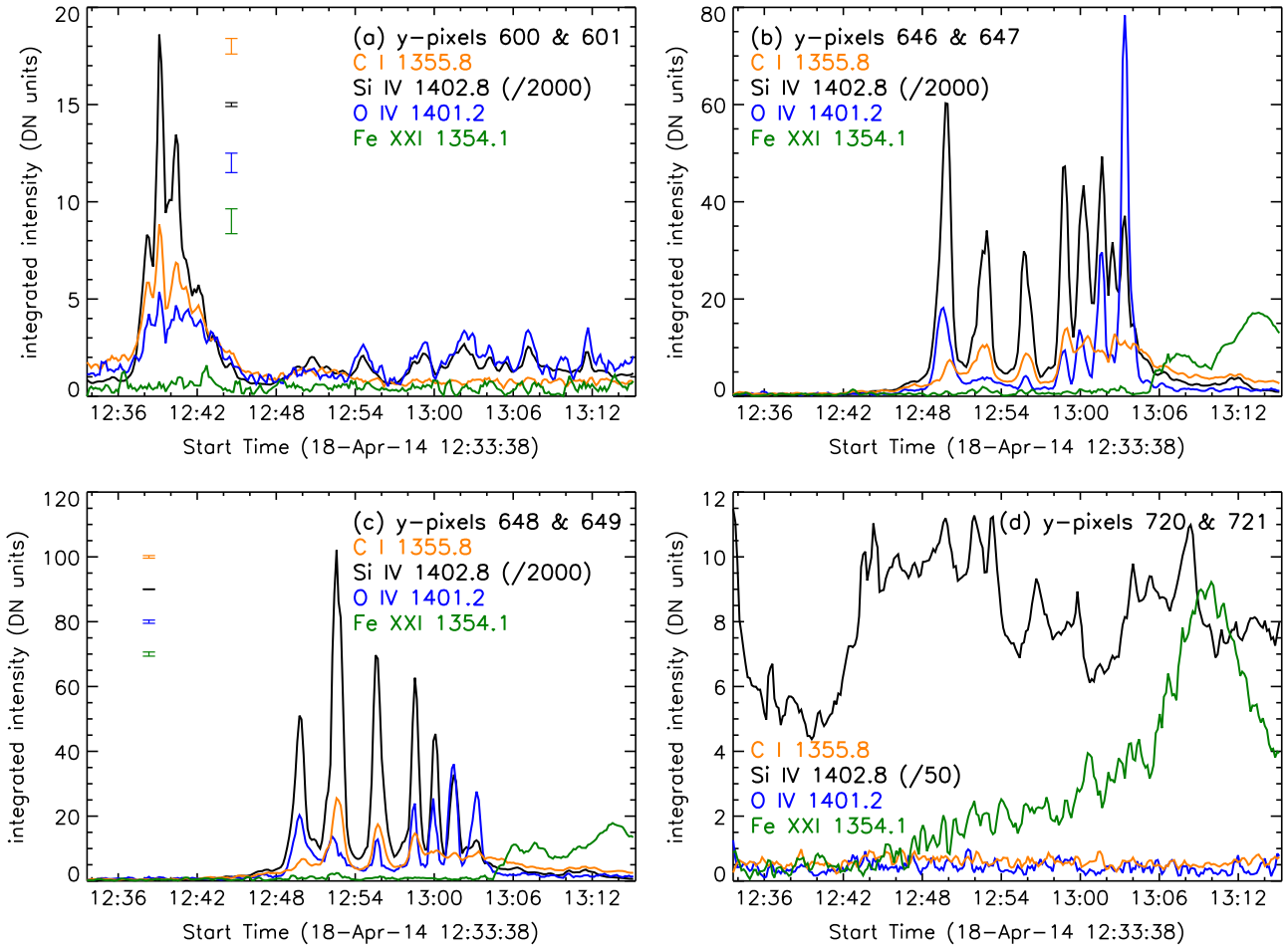

Figure 6. Light curves derived from four different 0.″333 × 0.″333 spatial locations along the *IRIS* slit. Frame (a) corresponds to an area outside the ribbon, at the lower yellow tick mark in Figure 1. Frames (b) and (c) correspond to areas within the flare ribbon, inside the blue box in Figure 1. Frame (d) corresponds to an area outside the ribbon, at the upper yellow tick mark in Figure 1. Integrated intensities of four emission lines (along with error bars indicating uncertainties in frames (a) and (c)) are color coded as indicated in each frame, where the *y*-pixels indicate the two 0.″333 × 0.″166 slit spatial pixels over which the spectra were averaged to derive the displayed light curves. Note that the Si IV intensities are reduced by factors indicated in each frame. These show the evolution at fixed locations on the solar disk that are tracked by the *IRIS* slit. Quasi-periodic fluctuations are bright and easily visible in the C I, Si IV, and O IV emission from the ribbon (frames (b) and (c)).

3. RESULTS

We report quasi-periodic intensity and velocity fluctuations in *IRIS* FUV spectra of chromospheric and transition region line emission from a flare ribbon, along with chromospheric evaporation during the flare's impulsive phase. The observed fluctuations indicate that the chromosphere and transition region are involved in the flare before Fe XXI emission appears.

3.1. Quasi-periodic fluctuations

Chromospheric and transition region lines observed by *IRIS* exhibit quasi-periodic fluctuations in the flare ribbon. These are evident in the spacetime "images" shown in Figures 3 and 5, and in the C I, Si IV, and O IV light curves shown in Figures 6(b), (c); Fe XXI light curves are overplotted to show the simultaneous evolution of emission from the flare (11 MK) plasma. Each frame in Figure 6 shows light curves from a different 0.″333 × 0.″333 spatial location along the *IRIS* slit. Frame (a) corresponds to an area outside the ribbon, at the lower yellow tick mark in Figure 1. Frames (b) and (c) correspond to areas within the flare ribbon, inside the blue box in Figure 1. Frame (d) corresponds to an area outside the ribbon, at the upper yellow tick mark in Figure 1. Integrated intensities of four emission lines are color coded as indicated in each frame, where the *y*-pixels indicate the two 0.″333 × 0.″166 slit spatial pixels over which the spectra were averaged to derive the displayed light curves. Note that the Si IV intensities are reduced by factors indicated in each frame. The color-coded uncertainties indicated in frames (a) and (c) correspond to twice the 1-sigma scatter in the line intensities during an interval of relatively small intensity variation (13:20:36–13:36:15 UT). These light curves show the evolution of UV line emission at fixed locations on the solar disk that are tracked by the *IRIS* slit to compensate for solar rotation. This tells us how the chromospheric, transition region, and flare emissions evolve in these small fields of view on timescales of 9.4 s. The Fe XXI light curves show some fluctuations, but if quasi-periodic behavior is present in these it is far less obvious than in the light curves of C I, Si IV, and O IV. Quasi-periodic fluctuations are possibly also evident outside the ribbon (frame (a)).

We determined the times at which the various intensity peaks occur in the light curves of Figures 6(b), (c) by fitting the curves with a series of Gaussian profiles. This yielded the times at which the various peaks occur to better than the 9.4 s time resolution of the observations. The time differences between

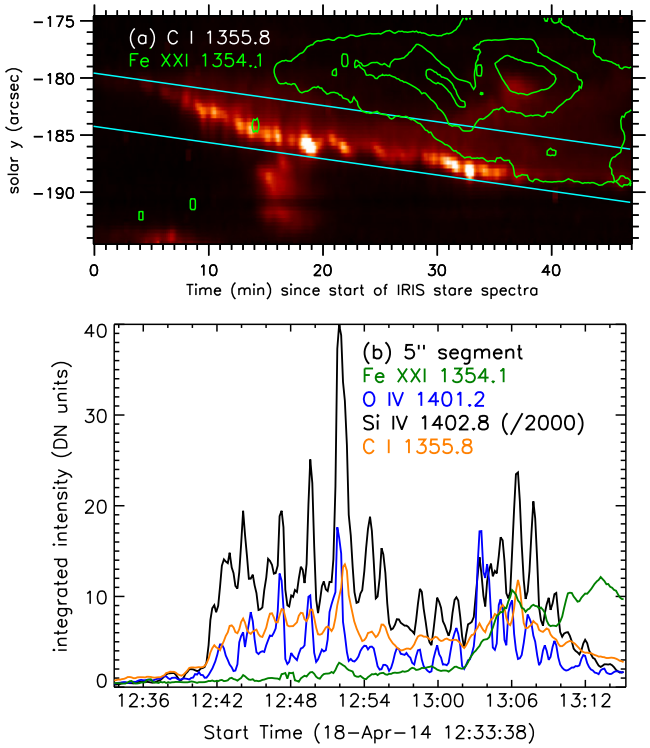

Figure 7. (a) Space vs. time C I 1355.8 Å intensity image with parallel blue lines to delineate the 5″ slit segment over which we average the southward-drifting ribbon's light curves shown in (b). Also shown in (a) are intensity contours of Fe XXI at 15%, 45%, and 75% of the maximum value in the array. We shift the 5″ segment southward about 12″/hr to track the southward drift of the ribbon. The light curves in (b), which show fluctuations, are composites of those in Figures 6(b), (c) as well as those outlined in frame (a).

successive peaks are somewhat variable, which is why we refer to them as "quasi-periodic." The quasi-periods are longer by nearly a factor of 2 for the first 4 intensity peaks than they are for the last 4 intensity peaks, changing from the longer value to the shorter value at the 4th peak in the series. We designate P_L as the "long quasi-period" and P_S as the "short quasi-period." For C I we obtain P_L(C I) = 170.0 ± 16.7 s and P_S(C I) = 92.8 ± 5.9 s, where the uncertainties cover the full range of calculated intervals between successive peaks. Similarly, for Si IV we obtain P_L(Si IV) = 176.4 ± 6.3 s and P_S(Si IV) = 90.9 ± 3.7 s, and for O IV we obtain P_L(O IV) = 175.6 ± 32.3 s and P_S(O IV) = 97.0 ± 8.5 s. Although it is straightforward to calculate P_L/P_S for C I (1.83 ± 0.21), Si IV (1.94 ± 0.11), and O IV (1.81 ± 0.37), it is uncertain whether these correspond to a shift from 1st to 2nd harmonic particularly in light of the variable intervals between intensity peaks. For the light curves in Figure 6(b) we derive quasi-periods comparable to those derived above, namely, P_L(C I) = 173.0 ± 27.2 s, P_S(C I) = 77.2 ± 16.6 s; P_L(Si IV) = 181.6 ± 5.8 s, P_S(Si IV) = 85.0 ± 2.5 s (with an additional, even shorter quasi-period of 50.4 ± 1.9 s); and P_L(O IV) = 185.2 ± 13.8 s, P_S(O IV) = 94.0 ± 14.2 s.

We examined the evolution of the average UV emission from the southward drifting section of ribbon seen in the slit by averaging the *IRIS* spectra from a 5″ slit segment that we shifted southward in time to follow the ribbon's movement. This 5″ slit segment is located between the solid blue lines in Figure 7(a); the negative slope of the parallel lines indicates the southward drift. Figure 7(b) shows light curves for the same four lines shown in Figure 6, averaged over the 5″ segment of the *IRIS* slit outlined in Figure 7(a). Each of these light curves corresponds to a composite of 15 light curves like those in Figures 6(b), (c), and includes more than 20 intensity peaks. These peaks represent a superposition of spatial and temporal variations in emission line intensity, likely ultimately due to a complex superposition of spatial and temporal variations in coronal energy release.

Figures 3, 5, 6, and 7 show that the C I, Si IV, and O IV emission brightens and exhibits quasi-periodic fluctuations before significant Fe XXI emission appears above the background noise. Fe XXI does show some variability after the chromospheric and transition region lines show quasi-periodic fluctuations, but the Fe XXI variations are neither as spiky nor as pronounced as are those in the C I, Si IV, and O IV emission, and they do not visually appear to be quasi-periodic. Thus, although quasi-periodic fluctuations in intensity and/or velocity have been reported in line emission of some flares observed with the Bragg Crystal Spectrometer (Culhane et al. 1991) aboard *Yohkoh* (Mariska 2006) and with the SUMER (Wilhelm et al. 1995) spectrometer aboard *Solar and Heliospheric Observatory* (Kliem et al. 2002; Wang et al. 2003; Wang 2011), we do not report them in this work. This may be because the *IRIS* slit was not pointed at the location where the flare actually began, or at the location where the ribbon became brightest.

We note that there are hints of brightenings in the Fe XXI emission in the light curves of Figures 6(b), (c) and Figure 7(b) during some of the peaks in the C I, Si IV, and O IV fluctuations; see, for example, the brightening around 12:52 UT. However, a close examination of the spectra at those locations in those exposures reveals that the emission attributed to Fe XXI is most likely due to Si II at 1353.718 Å and/or Fe II 1354.013 Å. Although we fit these lines separately from the Fe XXI line, their weakness (even though they do become brighter during the chromospheric and transition region fluctuation peaks) combined with noise in the vicinity of the absent Fe XXI line (whose fit we did not disable because we seek to determine when the Fe XXI emission reliably first appears) can lead to profile fits that suggest the presence of weak Fe XXI emission. We point this out to underscore the noise in the plots (particularly when a sought-after line is absent), and to confirm the cautionary words of Young et al. (2015) regarding possible blends with the Fe XXI line.

Figure 8 shows relative Doppler velocities derived for C I, Si IV, O IV, and Fe XXI, displayed along with their respective light curves, in the 0.″333 × 0.″333 field of view (FOV) comprised of *IRIS* slit pixels 648 and 649 within the flare ribbon. These show the evolution at a fixed location on the solar disk that is tracked by the *IRIS* slit. Positive velocities correspond to redshifted wavelengths (downward motion), while negative velocities correspond to blueshifted wavelengths (upward motion). Note that we have reduced the Fe XXI velocities by a factor of 10 to enhance visibility, and display those velocities only for exposures in which the line's intensity continuously exceeds its pre-flare average by more than twice the scatter in the pre-flare noise (2-sigma); this occurs in exposures 198 (13:04:38 UT) and later, and is indicated with a vertical green line. The quasi-periodic fluctuations that are evident in the C I, Si IV, and O IV light curves are also evident in the velocity plots, although not as pronounced. The interval of quasi-periodic intensity fluctuations is dominated by redshifted emission. The downward velocities vary roughly in phase with

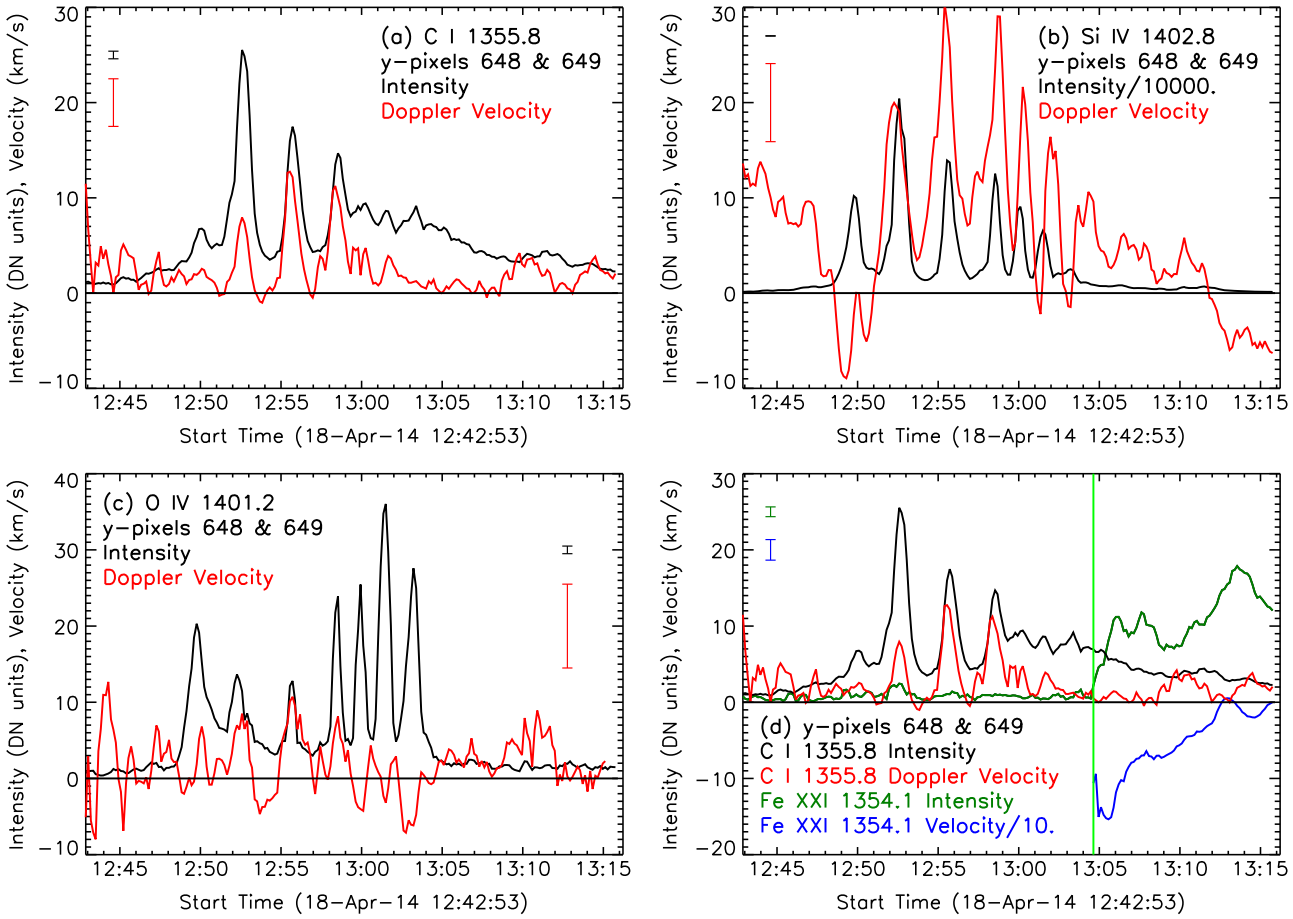

Figure 8. Light curves (black) and relative Doppler velocities (red), with corresponding measurement uncertainties indicated in each frame for four emission lines observed by *IRIS* in the 0.″333 × 0.″333 field of view fixed on the solar disk comprised of slit pixels 648 and 649 within the flare ribbon. In frame (d) we have reduced the Fe XXI velocity by a factor of 10 to enhance visibility, and display the velocities only for exposures in which the line's intensity continuously exceeds its pre-flare average by more than twice the scatter in the pre-flare noise (2σ); this occurs in exposure 198 (13:04:38 UT, indicated with a vertical green line) and later. The quasi-periodic fluctuations that are evident in the C I, Si IV, and O IV light curves are also evident in their velocity plots, although not as pronounced. The Fe XXI velocity is directed upward (blueshifted, negative velocity) -110 km s^{-1} when the line's intensity first becomes significant, at which time Si IV shows redshifted emission corresponding to a downward (positive) velocity of 9.6 km s^{-1}, while C I and O IV show insignificant redshifts.

the intensities during the first four intensity spikes; after that, the Si IV velocities show that peak redshifts occur after the peak intensities, at least for the last two spikes in the series. The C I and O IV velocity measurements are too weak and noisy to discern a change in pattern during these later intensity peaks.

3.2. Chromospheric Evaporation

Although *GOES* soft X-ray light curves indicate that the flare started 2.5 minutes before the *IRIS* observations began, the flare appears to have started about 30″ east of where the *IRIS* slit was pointed (see Figure 1). When the *IRIS* observations began, no evidence of flare ribbons (injection sites of flare energy into the chromosphere) was seen in the SJI at the slit's pointing position. Further, the light curves of emission lines observed in spectra at the location in which the ribbon eventually appeared along the slit all show very low intensities (with no evidence of flare-like behavior) for the first 12 minutes of *IRIS* observations. See Figures 6(b), (c). This means that the *IRIS* slit observed a pristine portion of the solar atmosphere when its observing run began, i.e., an area that had not detectably participated in the earliest part of the flare. This enables us to investigate chromospheric evaporation in a portion of the flaring solar atmosphere that is unmodified by flare energy injection prior to our observations.

Figures 6(b), (c), Figures 7(a), (b), and Figure 8(d) show that the intensities of the C I, Si IV, and O IV lines all brightened (and fluctuated quasi-periodically) *before* the Fe XXI emission began its impulsive intensity rise. The Fe XXI intensity increased rapidly after the last of the fluctuating intensity peaks in Figures 6(b), (c) and Figure 8(d). This indicates that for the small pristine fields of view (averaged pixel sizes 0.″333 × 0.″333) observed by the *IRIS* slit along the flare ribbon, flare-related activity began in the chromosphere before sufficient heating occurred to produce Fe XXI emission ($T \approx 11$ MK). For *IRIS* slit pixels 648 and 649 (Figures 6(c) and 8), we see that when the Fe XXI flare emission *did* finally appear (13:04:38 UT), the line's profile was shifted entirely blueward by an amount that corresponded to upward velocity around -110 km s^{-1}. This is the classic signature of chromospheric evaporation. At the same time, Si IV showed redshifted emission corresponding to a downward velocity of 9.6 km s^{-1}, consistent with explosive chromospheric evaporation, while C I and O IV showed insignificant redshifts corresponding to downward velocities less than 1 km s^{-1}. Two exposures later (13:04:57 UT) the Fe XXI profile showed its largest blueshift of -159 km s^{-1}, at

which time the Si IV profile showed a downward velocity of 4.9 km s^{-1}, O IV showed an insignificant downward velocity of 2.6 km s^{-1}, and C I showed no significant shift. It is possible that the observed redshifted emission in Si IV, but not in O IV, may be a result of high density in the redshifted plasma, causing collisional de-excitation of the upper levels of O IV.

A similar pattern is observed in the other slit spatial pixels within the ribbon: the Fe XXI profile is entirely blueshifted (by an average upward velocity around -100 km s^{-1}) when the line first appears, and remains entirely blueshifted while its upward velocity increases (to an average around -154 km s^{-1}) during the next several exposures before decreasing to zero near the time of maximum intensity. The corresponding average Si IV velocities ($+8.3$ and $+7.0$ km s^{-1}) are directed downward, which indicates that evaporation is explosive when Fe XXI emission first appears as well as when it reaches its maximum upward velocity.

We examined spectra in the *IRIS* waveband that includes the Fe XII forbidden line at 1349.40 Å (formed at typical coronal temperature around 1.6 MK) in hopes of monitoring the flare atmosphere's evolution at temperatures between those in the transition region and those in flare plasma. Brosius & Holman (2007), for example, used EUV spectra from the Coronal Diagnostic Spectrometer (Harrison et al. 1995) to determine that explosive evaporation occurred in a flare-like transient brightening that was separated from the primary flare brightening based in part on blueshifted emission in the Si XII line at 520.7 Å ($T \approx 2$ MK) observed simultaneously and cospatially with redshifted emission in chromospheric (He I) and transition region (O V) line emission. Here, we employed a variety of averaging approaches in order to optimize the detection of the weak Fe XII line, but found it only in spectra that were too heavily averaged over time and space to be useful for investigating rapid flare evolution in the ribbon.

4. DISCUSSION AND INTERPRETATION

Because the *IRIS* slit tracked its target to compensate for solar rotation, we are able to monitor the evolution of the flaring atmosphere within a small but constant spatial area on the Sun. The *IRIS* stare spectra show quasi-periodic fluctuations in the intensities and relative Doppler velocities of chromospheric and transition region lines in slit pixels within the flare ribbon. The fluctuations began about 18 minutes before Fe XXI emission was detected in the same slit pixels. The C I 1355.8, Si IV 1402.8, and O IV 1401.2 Å lines all very clearly show quasi-periodic fluctuations in their intensities. They also show, although less clearly, fluctuations in their relative Doppler velocities. Inglis & Nakariakov (2009) point out that rarely more than 4 or 5 complete cycles of flare fluctuations are observed. Here we observe four complete repetitions for each of a longer quasi-period (≈171 s) followed by a shorter quasi-period (≈95 s). This demonstrates that two distinct quasi-periods can be detected within small ($0\farcs333 \times 0\farcs333$) fields of view, and that the two quasi-periods occur sequentially, not simultaneously.

The largest intensity peaks observed in the C I, Si IV, and O IV fluctuations are $\gtrsim$40 times brighter than the average intensities before the start of the fluctuations, and $\sim$ 10 times brighter than the intensities between the peaks during the fluctuations. This is the kind of brightening expected (e.g., Fisher et al. 1985) and observed (e.g., Brosius & Phillips 2004) in transition region line emission when beams of nonthermal particles impact the chromosphere and heat it rapidly. The observed redshifts in chromospheric and transition region line emission indicate the kind of downflows expected in the case of explosive chromospheric evaporation. However, because no Fe XXI emission is detected until the fluctuations have ceased, we cannot use Fe XXI velocity measurements to confirm this conclusion. Further, the Fe XII forbidden line observed by *IRIS* is too weak to provide velocity measurements on spatial and temporal scales that would help to confirm this conclusion.

The observed C I, Si IV, and O IV fluctuations provide evidence for bursty reconnection. In this scenario, each episode of intensity increase indicates a coronal reconnection event followed by energy injection into the chromosphere (at the location of the flare ribbon observed by *IRIS*) by accelerated particles. Each such episode can perhaps be thought of as a failed flare in the sense that no emission at temperatures characteristic of flares is produced, i.e., no Fe XXI emission is observed. The fact that the fluctuations are associated primarily with redshifts in the line emission suggests that chromospheric evaporation may be occurring explosively at these times, but that upward moving material is at temperatures to which *IRIS* is not sensitive.

Previous observations of chromospheric and transition region brightenings prior to the appearance of hot flare emission were interpreted in terms of energy injection into the chromosphere by nonthermal particle beams (Cauzzi et al. 1995; Brosius & Phillips 2004; Brosius & Holman 2009), and we draw the same conclusion here. Eventually the flare succeeds, as revealed by the appearance of blueshifted Fe XXI emission in which the initial upward velocity (when the line is first detected) is ≈ -110 km s^{-1} and the maximum upward velocity (several exposures later) is ≈ -150 km s^{-1}. This is the classic signature of chromospheric evaporation. Because the bright Si IV emission shows simultaneous downward velocities between 4 and 12 km s^{-1}, the chromospheric evaporation is likely explosive (Fisher et al. 1985; Allred et al. 2005; Milligan et al. 2006a, 2006b; Brosius 2009). The C I and O IV lines show insignificant velocities at the same time, and so provide no conclusive support either for or against this conclusion.

We visually inspected line profile fits to more than 100 ribbon spectra that contain the Fe XXI line at and before the Fe XXI intensity peak in an attempt to search for evidence of secondary blueshifted components to the Fe XXI emission. Brosius (2013a) interpreted secondary blueshifted components to the Fe XXIII line at 263.8 Å observed during a flare in rapid cadence stare mode by the Extreme-ultraviolet Imaging Spectrometer (EIS; Culhane et al. 2007) in terms of chromospheric evaporation in successive strands within a flare loop envelope. In this scenario (Hori et al. 1998; Doschek & Warren 2005; Warren & Doschek 2005; Warren 2006), the whole line profile is expected to be blueshifted when evaporation occurs in only a single, resolved strand; once the strand is filled, evaporation stops and the flare line should appear to be at rest. If more than one strand is observed within a given spectrometer's FOV (or its spatial resolution), the whole line profile will be blueshifted while the first strand fills with evaporating material, but after the first strand has filled and subsequent strands are activated, emission from the newly activated strands will appear as secondary blueshifted components to the rest emission from the first strand (which has already been filled and in which evaporation has ceased). We speculate that because no secondary blueshifted components

are observed attached to any of the stationary Fe XXI profiles, perhaps the *IRIS* spatial resolution (which, at 0.″333, is better than that of EIS at 3.″0 to 4.″0) is adequate to resolve loop strands in these observations. (An additional complication with the EIS observations is jitter in the spacecraft pointing, which Mariska (2010) finds to be 2–3 arcsec at most over a 1-hour period.)

5. SUMMARY AND CONCLUSIONS

Rapid cadence (9.4 s) FUV stare spectra of a flare ribbon observed by *IRIS* reveal quasi-periodic intensity and velocity fluctuations in chromospheric and transition region line emission prior to the appearance of Fe XXI line emission. Seven intensity peaks were observed in small (0.″333 × 0.″333) tracked spatial locations in the ribbon. The first four peaks show variable time separations around 171 s, and the last four peaks show variable time separations around 95 s. Fluctuations observed in the Doppler velocities are not as pronounced as those in the intensities. The Fe XXI intensity increased rapidly and impulsively after the quasi-periodic fluctuations in chromospheric and transition region lines. The entire Fe XXI line profile was blueshifted when the line first appeared, corresponding to an upward velocity around -100 km s^{-1}; this upward velocity increased to a maximum of about -150 km s^{-1} before diminishing to zero around the time of maximum intensity. Simultaneous, cospatial velocities observed with Si IV were directed downward, consistent with explosive chromospheric evaporation. During this flare the Fe XXI line's profile is well fit with only one Gaussian component that is either wholly blueshifted or wholly at rest; no significant secondary blueshifted or redshifted components are observed. This leads us to speculate that *IRIS* may have sufficient spatial resolution to resolve loop strands in these flare observations. We derive a rest wavelength of 1354.0714 ± 0.0108 Å for the forbidden line of Fe XXI in *IRIS* spectra, a low-uncertainty value that is consistent with previous measurements.

IRIS is a NASA small explorer mission developed and operated by LMSAL and partner institutions with mission operations executed at NASA Ames Research center and major contributions to downlink communications funded by the Norwegian Space Center (NSC, Norway) through an ESA PRODEX contract. CHIANTI is a collaborative project involving George Mason University (USA), the University of Michigan (USA), and the University of Cambridge (UK).

REFERENCES

Allred, J. C., Hawley, S. L., Abbett, W. P., & Carlsson, M. 2005, ApJ, 630, 573
Antonucci, E., Babriel, A. H., Acton, L. W., et al. 1982, SoPh, 78, 107
Antonucci, E., Alexander, D., Culhane, J. L., et al. 1999, in The Many Faces of the Sun, ed. K. T. Strong, J. L. R. saba, B. M. Haisch, & J. T. Schmelz (New York: Springer), 331
Bornmann, P. L. 1999, in The Many Faces of the Sun, ed. K. T. Strong, J. L. R. Saba, B. M. Haisch, & J. T. Schmelz (New York: Springer), 301
Brosius, J. W. 2003, ApJ, 586, 1417
Brosius, J. W. 2009, ApJ, 701, 1209
Brosius, J. W. 2013a, ApJ, 762, 133
Brosius, J. W. 2013b, ApJ, 777, 135
Brosius, J. W., & Holman, G. D. 2007, ApJL, 659, L73
Brosius, J. W., & Holman, G. D. 2009, ApJ, 692, 492
Brosius, J. W., & Phillips, K. J. H. 2004, ApJ, 613, 580
Carmichael, H. 1964, in Physics of Solar Flares, ed. W. N. Hess (Washington, D.C.: NASA, Science and Technical Information Division), 451
Cauzzi, G., Falchi, A., Falciani, R., et al. 1995, A&A, 299, 611
Culhane, J. L., Hiei, E., Doschek, G. A., et al. 1991, SoPh, 136, 89
Culhane, J. L., Harra, L. K., James, A. M., et al. 2007, SoPh, 243, 19
De Pontieu, B., Title, A. M., Lemen, J. R., et al. 2014, SoPh, 289, 2733
Dere, K. P., Landi, E., Mason, H. E., Monsignori-Fossi, B. C., & Young, P. R. 1997, A&AS, 125, 149
Doschek, G. A. 1983, SoPh, 86, 49
Doschek, G. A., & Warren, H. P. 2005, ApJ, 629, 1150
Doschek, G. A., Warren, H. P., & Young, P. R. 2013, ApJ, 767, 55
Edlen, B. 1963, RPPh, 26, 181
Fang, C., Tang, Y.-H., & Xu, Z. 2006, ChJAA, 6, 597
Feldman, U., Curdt, W., Landi, E., & Wilhelm, K. 2000, ApJ, 544, 508
Fisher, G. H., Canfield, R. C., & McClymont, A. N. 1985, ApJ, 289, 425
Fletcher, L., Dennis, B. R., Hudson, H. S., et al. 2011, SSRv, 159, 19
Fletcher, L., & Hudson, H. S. 2008, ApJ, 675, 1645
Haerendel, G. 2009, ApJ, 707, 903
Harrison, R. A., et al. 1995, SoPh, 162, 233
Haughan, S. V. H. 1997, CDS Software Note No. 47 http://www.mssl.ucl.ac.uk/surf/sswdoc/local_copy/cds/cds_guide/software_notes.html
Hirayama, T. 1974, SoPh, 34, 323
Hori, K., Yokoyama, T., Kosugi, T., & Shibata, K. 1998, ApJ, 500, 492
Inglis, A. R., & Nakariakov, V. M. 2009, A&A, 493, 259
Jackiewicz, J., & Balasubramaniam, K. S. 2013, ApJ, 765, 15
Kelly, R. L. 1987, JPCRD, 16, 1
Keys, P. H., Jess, D. B., Mathioudakis, M., & Keenan, F. P. 2011, A&A, 529, A127
Kliem, B., Dammasch, I. E., Curdt, W., & Wilhelm, K. 2002, ApJL, 568, L61
Kopp, R. A., & Pneuman, G. W. 1976, SoPh, 50, 85
Landi, E., Young, P. R., Dere, K. P., Del Zanna, G., & Mason, H. E. 2013, ApJ, 763, 86
Mariska, J. T. 2006, ApJ, 639, 484
Mariska, J. T. 2010, EIS Software Note, 9 http://hesperia.gsfc.nasa.gov/ssw/hinode/eis/doc/eis_notes/09_POINTING/eis_swnote_09.pdf
Mariska, J. T., Doschek, G. A., & Bentley, R. D. 1993, ApJ, 419, 418
McAteer, R. T. J., Gallagher, P. T., & Brown, D. S. 2005, ApJ, 620, 1101
McIntosh, S. W., de Pontieu, B., Hansteen, V., Carlsson, M., & Boerner, P. 2014, A User's Guide to *IRIS* Data Retrieval, Reduction & Analysis, http://www.iris.lmsal.com/documents.html
Milligan, R. O., Gallagher, P. T., Mathioudakis, M., & Keenan, F. P. 2006a, ApJL, 642, L169
Milligan, R. O., Gallagher, P. T., Mathioudakis, M., et al. 2006b, ApJL, 638, L117
Nakariakov, V. M., et al. 2010, PPCF, 52, 124009
Nakariakov, V. M., & Melnikov, V. F. 2009, SSRv, 149, 119
Nave, G., & Johansson, S. 2013, ApJS, 204, 1
Neupert, W. M. 1968, ApJL, 153, L59
Ni, L., Kliem, B., Liu, J., & Wu, N. 2015, ApJ, 799, 79
Sandlin, G. D., Brueckner, G. E., & Tousey, R. 1977, ApJ, 214, 898
Shirai, T., Sugar, J., Musgrove, A., & Wiese, W. L. 2000, JPCRD, Monograph No. 8
Sturrock, P. A. 1968, in IAU Symp. 35, Structure and Development of Solar Active Regions, ed. K. O. Kiepenheuer (Dordrecht: Reidel)
Teriaca, L., Falchi, A., Cauzzi, G., et al. 2003, ApJ, 588, 596
Teriaca, L., Falchi, A., Falciani, R., Cauzzi, G., & Maltagliati, L. 2006, A&A, 455, 1123
Tian, H., Li, G., Reeves, K. K., et al. 2014, ApJL, 797, L14
Wang, H., Qiu, J., Denker, C., et al. 2000, ApJ, 542, 1080
Wang, T. J. 2011, SSRv, 158, 397
Wang, T. J., Solanki, S. K., Curdt, W., et al. 2003, A&A, 406, 1105
Warren, H. P. 2006, ApJ, 637, 522
Warren, H. P., & Doschek, G. A. 2005, ApJL, 618, L157
Wilhelm, K., Curdt, W., Marsch, E., et al. 1995, SoPh, 162, 189
Young, P. R., Doschek, G. A., Warren, H. P., & Hara, H. 2013, ApJ, 766, 127
Young, P. R., Tian, H., & Jaeggli, S. 2015, ApJ, 799, 218